Conductor-Based Modeling of a Single-Tooth Winding for EMI Simulation

Hujun Peng, Yue Yu, and Kay Hameyer, *Senior Member, IEEE*

***Abstract*—A universal gray box model is proposed for the single-tooth winding of a permanent magnet synchronous machine across a wide frequency range. The proposed model facilitates the analysis of voltage distribution within the winding under inverter-fed operations. Compared to the state-of-the-art, the proposed model considers a frequency-dependent mutual impedance between various conductors within the winding. Furthermore, the capacitive and inductive coupling between different turns and between turns and the winding housing is considered in the model. The parameterization process is carried out using impedance measurements. Thereby, the model parameters are optimized using a genetic algorithm. The the model is first validated in the frequency domain. Then, an impulse generator consisting of silicon carbide power modules is used to validate the accuracy of the voltage distribution along the single-tooth winding under different conditions. A maximum relative error of 6.5% is observed between the simulated and measured voltage peaks along the single-tooth winding at different switching frequencies and du/dt conditions.**

***Index Terms*—Gray box model, high-frequency modeling, single-tooth winding, transient overvoltage.**

I. Introduction

SINGLE-TOOTH windings are gaining increased prominence in electrical machines due to their ability to achieve significantly higher copper fill factors and shorter end windings. This winding choice improves efficiency and enhances the power density of electrical machines, as highlighted in previous studies [1], [2]. On the other side, technological advances have paved the way for integrating fast-switching metal-oxide field-effect transistors (MOSFETs) in high-power applications. Emerging materials such as silicon carbide (SiC) and gallium nitride lead to higher efficiency for automotive applications. These advanced MOSFET components exhibit a short switching time or high slew rate (SR) [3], which induces voltage oscillations at winding terminals and along the winding itself [4]. This voltage oscillation phenomenon is particularly pronounced when employing single-tooth windings [5], [6]. As a result, the interplay between single-tooth windings and these new types of MOSFETs introduces notable challenges if used in the electric power train.

Manuscript received 2 February 2024; revised 26 March 2024; accepted 17 May 2024. Date of publication 21 May 2024; date of current version 16 July 2024. Recommended for publication by Associate Editor F. Costa. *(Corresponding author: Hujun Peng.)*

The authors are with the Institute of Electrical Machines (IEM), RWTH Aachen University, 52062 Aachen, Germany (e-mail: hujun.peng@iem.rwth-aachen.de).

Color versions of one or more figures in this article are available at https://doi.org/10.1109/TPEL.2024.3403669.

Digital Object Identifier 10.1109/TPEL.2024.3403669

The existing literature emphasizes that the maximum voltage in electrical machines can reach two times the dc-link voltage due to the impedance mismatch between power cables and the electrical machine [7], [8], [9]. In cases of a double-pulsing effect, the maximum voltage can surge to four times the dc-link voltage. A commonly adopted strategy to improve the safety and reliability of electrical machines is to overdesign the thickness of insulation layers. However, the insulation overdesign could be circumvented if the voltage peaks between windings and the motor housing can be estimated accurately [10]. For this purpose, a high-frequency model of windings is proposed to predict the maximum voltage stress between the winding and housing.

The high-frequency models can be categorized into the white box model and the gray box model. The white box model is based on the transmission-line model [11], which estimates the voltage distribution using equivalent electrical circuits. Researchers in [12], [13], and [14] proposed white box models for coils instead of the entire electrical machine. In Zheng et al.'s [15] work, a model based on motor winding turns is developed for enhanced voltage prediction. However, this model did not consider the skin and proximity effects in the high-frequency range. Furthermore, in Sundeep et al.'s [16] work, the frequency-dependent mutual inductive coupling among neighboring conductors is modeled using current-controlled voltage sources. This approach represents the state-of-the-art white box modeling of electrical machines. The white box model can be implemented before prototyping the electrical machines, provided that the geometry and material data necessary for the finite element analysis are available. However, implementing these models requires a significant effort. The requirement for frequency-dependent permeability up to several mega-Hertz is mentioned in Stoll's [17] work, and the high computational demands also present challenges.

In contrast to the white box modeling method, classical gray box modeling analyzes interactions outside of machines and is used for existing machines. The parameterization process is based on measured impedance spectra and optimization algorithms, as described in [18] and [19].

The state-of-the-art gray box models are well-developed for high-frequency modeling of electrical machines. In Karakaşll et al.'s [20] work, a gray box model for an induction machine is presented, incorporating the complexities of capacitive and inductive coupling between phases. The authors in [21] and [22] introduced high-frequency gray box models that account for mutual inductance between different coils of electrical machines. Moreover, the frequency-dependency of mutual inductance between phases is implemented by the authors in [23] and [24]. However, the gray box models have not been used at the conductor level. Furthermore, while existing gray box modeling offers the advantage of requiring less modeling and parameterization effort, it cannot estimate the detailed voltage distribution as well as the white box models. Such estimation is crucial for the design of insulation layers, as mentioned earlier. In order to address the gap in the gray box modeling of the single-tooth winding, this work contains the following contributions.

1) The gray box model of a single-tooth winding is implemented, enabling the prediction of the voltage distribution along the single-tooth winding.
2) The proposed gray box model considers the frequency-dependent mutual impedance between various turn conductors.
3) The proposed gray box model is validated in the frequency domain up to 10 MHz, with an averaged relative error lower than 10%.
4) The proposed gray box model is validated in the time domain through measurements on a test bench, accounting for various SRs and switching frequencies. The averaged relative error is 2.46% for the peak value of the ground-to-turn voltage and 3.95% for the oscillation frequency during the switching processes of power electronic devices.

The rest of this article is organized as follows. Section II provides an overview of impedance measurement involving the measurement configuration, results, and a preliminary experiment. Section III introduces the gray box modeling method. Section IV validates the model in the frequency domain, comparing the impedance spectra of different topologies modeled and measured. Subsequently, Section V presents the validation results of the gray box model in the time domain based on test bench measurements. Finally, Section VI concludes this article.

II. Impedance Measurement Setup and Corresponding Results

Fig. 1(a) presents the single-tooth winding to be modeled. Fig. 1(b) illustrates the structure of the modeled tooth winding. Measurements are conducted at various points between the single-tooth winding terminals and the housing to improve modeling precision. The following sections offer a comprehensive overview of the measurement setup and the results obtained from the impedance measurements. A preliminary experiment is also introduced to help analyze the high-frequency behaviors of the single-tooth winding.

A. Setup and Results of Measuring Impedance Spectra of the Single-Tooth Winding

The impedance analyzer "Keysight E4990 A" is used to measure the impedance spectra in the frequency range from 100 Hz to 10 MHz. In order to facilitate modeling analysis and subsequent parameter identification for the conductor-based model, each intermediate point between turns of the single-tooth

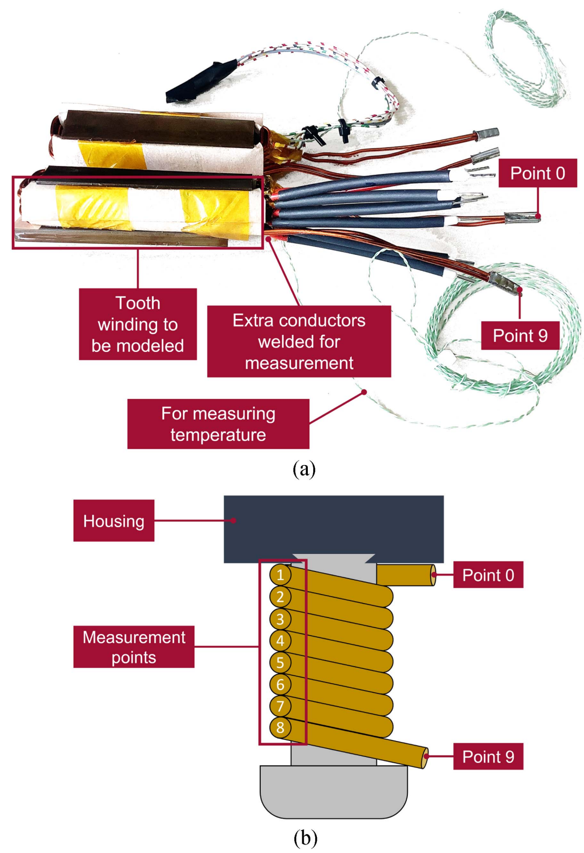

Fig. 1. Configuration of the single-tooth winding to be modeled. (a) Physical picture of the single-tooth winding with measurement points along the winding. (b) Schematic diagram of the single-tooth winding.

winding is assigned a numerical identifier ranging from 0 to 9. This sequential numbering was applied in ascending order from the beginning to the end of the winding, as depicted in Fig. 1(b). The impedance between distinct pacing points, called "turn-to-turn" impedance, is measured. The notation impedance "*i*-to-*j*" denotes the impedance between pacing point *i* and *j*. Furthermore, an additional measurement point was affixed to the housing, enabling the assessment of impedance between each turn and housing, referred to as "turn-to-gnd" impedance, at varying positions along the single-tooth winding.

Fig. 2 illustrates the results of these measurements, emphasizing the similarities observed between each turn. Such resemblances are anticipated, given the structural characteristics of a concentrated single-tooth winding. In the low-frequency range (under 1 MHz), the "turn-to-turn" impedance primarily exhibits inductive behavior, increasing with frequency. As the frequency continues to rise, the significant impact of parasitic capacitance is no longer negligible. The phase angle of the "turn-to-turn" impedance approaches $-90°$ at high frequencies above 5 MHz. Compared to that, the "turn-to-ground" impedance primarily reflects the characteristics of the insulation layer at low frequencies. With higher frequency, a peak-shaped protrusion in the phase angle of the "turn-to-ground" impedance above 3 MHz is observed, indicating inductive behavior. It is necessary to clarify whether this phenomenon results from the inductive behavior of

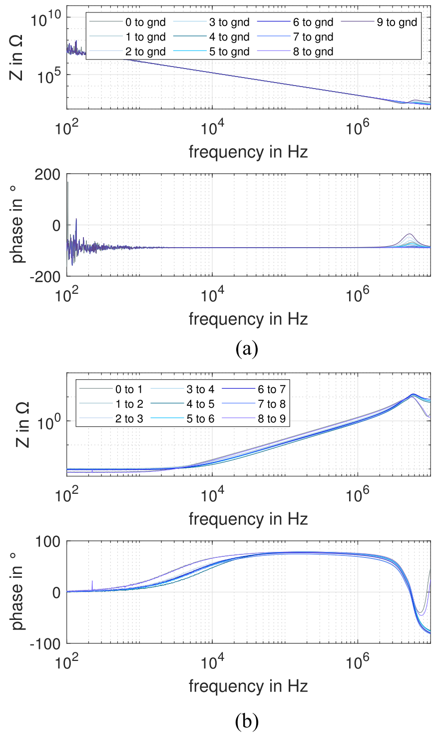

Fig. 2. Measured impedance spectra of the single-tooth winding for different topologies. (a) Common mode topologies "turn-to-gnd." (b) Differential mode topologies "turn-to-turn."

the copper conductors or the machine housing, which is made of iron materials. Thus, a preliminary experiment is designed in the following part.

B. Preliminary Experiment Using Stator Sheet Package

In the preliminary experiment, the impedance of a laminated core, exhibiting properties akin to the tooth winding housing, is initially measured. As shown in Fig. 3(a), contact points are symmetrically affixed to the laminated core through welding. Impedance measurements are conducted at various angles between a reference point and measurement points. The results in Fig. 3(b) indicate a significantly low impedance value at the laminated core, with relatively weak position dependence. Fig. 4(a) illustrates an adjusted experimental setup based on the stator pack, in which a cable is wound around a "tooth" of the laminated core to simulate the common mode behavior of a single-tooth winding. Similarly, the "turn-to-ground" impedance is measured and compared at various geometric angles. The findings in Fig. 4(b) indicate a minor position-dependent effect on impedance and nearly pure capacitive coupling behavior up to 3 MHz. A significant increase in phase angle is observed at around 5 MHz. Meanwhile, the value of the "turn-to-ground" impedance is about 100 Ω, significantly higher than the "housing" impedance at the same frequency range in Fig. 3(b). The observation suggests that the insulation layer between the winding and housing is the primary factor to consider during the modeling of the single-tooth winding, and the impedance due to the housing can be disregarded due to its much lower impedance amplitude.

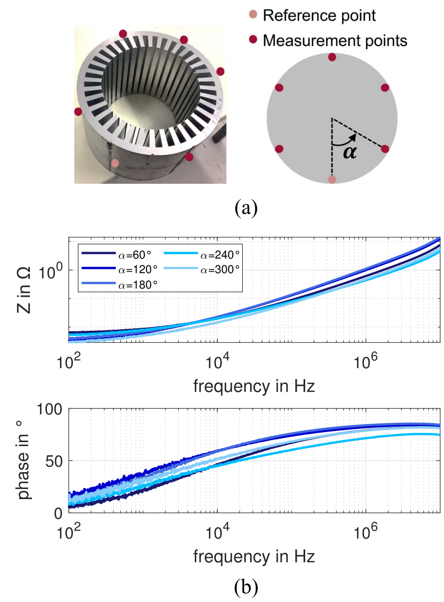

Fig. 3. Preliminary experiment to identify the position-irrelevance of the impedance in the stator sheet package. (a) Measurement setup. (b) Measured impedance spectra.

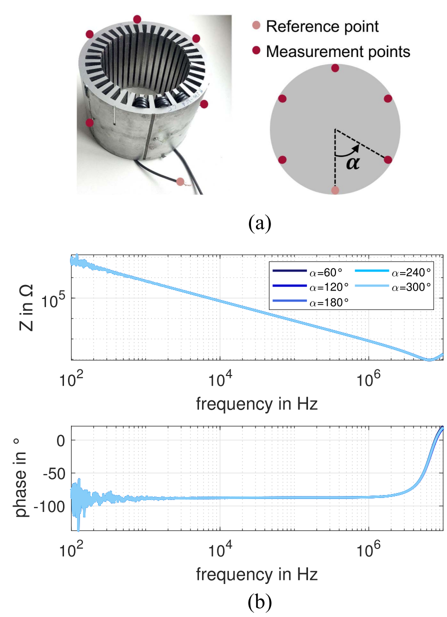

Fig. 4. Preliminary experiment for measuring the "turn-to-ground" impedance between a cable coil and the stator package housing. (a) Measurement setup. (b) Measured impedance spectra.

The following section will introduce a gray box model based on the measured impedance spectra of the single-tooth winding.

III. Setup of the Gray Box Model and the Parameter Fitting Program

A. Model Consisting of Π-Shaped Units

Based on the results of the experiment, the following considerations have been incorporated into the conductor-based model of the single-tooth winding.

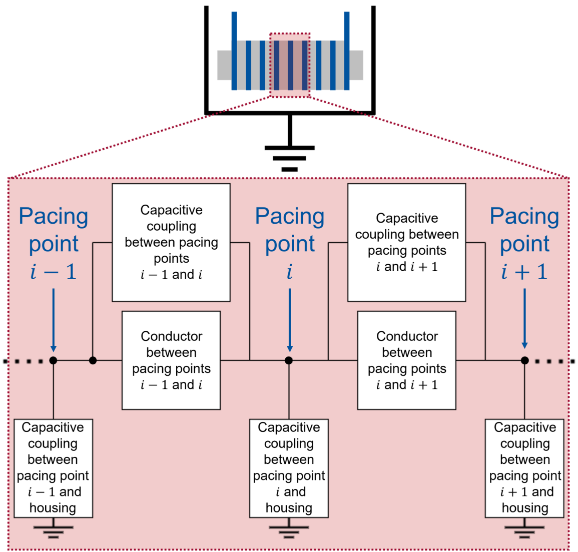

Fig. 5. Fundamental model structure with Π-shaped units between pacing points.

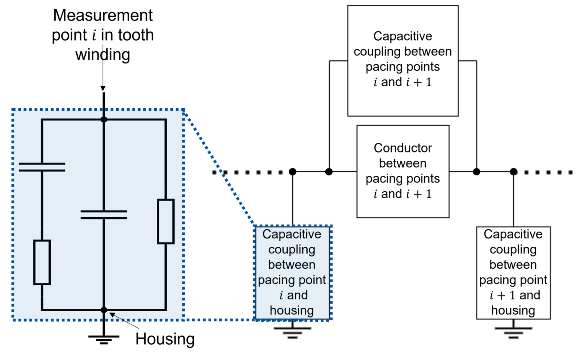

Fig. 6. Modeling of capacitive coupling between each turn conductor and the single-tooth winding housing.

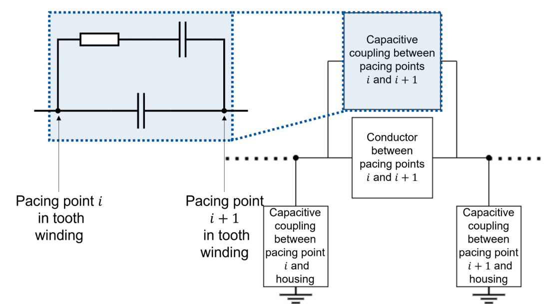

Fig. 7. Modeling of capacitive coupling between two neighboring conductor turns.

1) Frequency-dependent capacitive coupling between turns and housing.
2) Frequency-dependent capacitive coupling between neighboring turns.
3) Frequency-dependent skin effect in each turn.
4) Frequency-dependent proximity effect between turns.

Due to the frequency-dependent inductive and capacitive coupling, the classical telegrapher's equations cannot be used to determine the voltage distribution along the conductors of the single-tooth winding. Moreover, the individual turns are located in a nonevenly environment, so a theoretical equation for deriving the voltage potential distribution does not exist. Therefore, the gray box model with equivalent circuits is more suitable for considering the frequency-dependent and nonevenly environmental factors.

Primarily, the model structure of a single turn (between pacing points i and i+1) is introduced as the foundational design for the single-tooth winding. Leveraging the impedance properties observed in the single-tooth winding, as indicated by the results in Fig. 2, the entire winding structure can be constructed by replicating this fundamental unit. This essential, Π-shaped unit structure is presented in Fig. 5. The subsequent sections will introduce each substructure, modeled with a corresponding equivalent electrical circuit. It is crucial to highlight that inductive coupling among various turns will also be integrated.

B. *Modeling of the Capacitive Coupling Between Turns and Housing in the* Π*-Shaped Unit*

The experimental findings depicted in the preliminary experiment indicated that the inclusion of the motor housing's self-induction is unnecessary when modeling the capacitive coupling between the winding and housing. Consequently, our primary focus remains on modeling the insulation system of the single-tooth winding.

Illustrated in Fig. 6, the model structure delineates the capacitive coupling between measurement points i and the motor housing. This configuration captures the capacitive coupling between the winding and the housing. In order to model the capacitive coupling, a single resistor with notable resistance is initially selected. This choice serves to approximate the insulation dc resistance. The parasitic capacitance between the winding and housing is crucial when evaluating the insulation layer's performance at high frequencies. Therefore, a capacitor is connected in parallel with the insulation dc resistance in the model. This capacitor describes the capacitive coupling between turns and the housing without polarization losses. Besides, a parallel branch consisting of a resistor and a capacitor connected in series is applied to represent the capacitive coupling between turns and housing with polarization losses.

C. *Modeling of the Capacitive Coupling Between Turns in the* Π*-Shaped Unit*

For the capacitive coupling between neighboring turns in the winding, similar to the coupling model between turns and housing, the model incorporates two capacitors in parallel connection, one with and the other without a resistor, as illustrated in Fig. 7. The capacitive coupling between conductors not next to each other is indirectly considered through these neighboring capacitive couplings. In other words, capacitive coupling between conductors that are farther apart includes all capacitive coupling between neighboring conductors that are in between them.

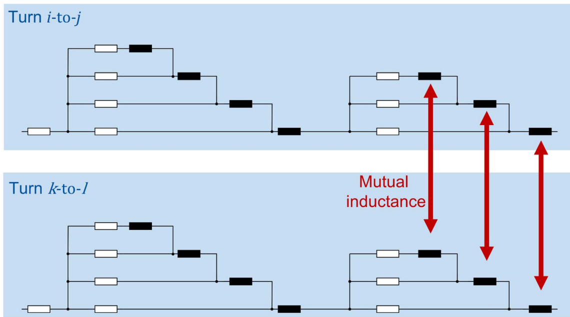

Fig. 8. Modeling of the inductive coupling between conductors of the single-tooth winding.

D. Modeling of the Inductive Coupling in and Between the Conductors of the Single-Tooth Winding

In order to model the frequency-dependent skin effect in each turn, the conductor-based model incorporates an *RL*-ladder structure, as shown in "Part-A" in Fig. 8. Nonetheless, the skin effect relates to the behavior of a single conductor. It is also crucial to consider the proximity effect between conductors of the single-tooth winding since it influences the impedance more strongly than the skin effect in conductors of the single-tooth winding. Considering these factors, a more detailed conductor-based model for the single-tooth winding is presented in Fig. 8. In the electrical circuit, each conductor consists of "Part-A" and "Part-B." "Part-A" incorporates a four-layer *RL*-ladder to approximate the skin effect in each conductor.

The segment "Part-B" integrates a three-layer *RL*-ladder network. This portion of the model is designed to characterize the proximity effect. Furthermore, the proximity effect encompasses inductive coupling across all layers between various turns, as illustrated using bidirectional arrows in Fig. 8. Each mutual inductance is described by using a matrix as follows:

$$\begin{bmatrix} \mathrm{L}_{11,k} & \mathrm{M}_{12,k} & \cdots & \mathrm{M}_{19,k} \\ \mathrm{M}_{21,k} & \mathrm{L}_{22,k} & \cdots & \mathrm{M}_{29,k} \\ \vdots & \vdots & \ddots & \vdots \\ \mathrm{M}_{91,k} & \mathrm{M}_{92,k} & \cdots & \mathrm{L}_{99,k} \end{bmatrix}$$

with

$$\mathrm{M}_{ij,k} = \mathrm{M}_{ji,k} \tag{1}$$

where k signifies the index of the layer number in *RL*-ladder network associated with the corresponding inductance in "Part-B," which varies from 1 to 3. The number 9 means that there are nine conductors in the single-tooth winding.

It has to be mentioned that the component parameters presented in Fig. 8 must satisfy the following constraints to promote the model parameter search.

1) For both "Part-A" and "Part-B," it is required that the resistance in the lower layers of the *RL*-ladder must be higher than in the upper layers. This requirement is essential to guarantee increased resistance with frequency attributed to the skin effect and proximity effect.
2) The coupling factors calculated for each mutual inductance should fall within the range of 0–1, reflecting the structure of the single-tooth winding.

E. Definition of the Cost Function for Searching the Model Parameters Using Optimization Algorithms

The parameters are identified using optimization algorithms, which minimize the difference between the modeled and measured impedance spectra. Here, a genetic algorithm is employed. Various measurement topologies are considered to define the cost function needed by the genetic algorithm.

The cost function in our work incorporates the deviations between simulated and measured values in impedance amplitude and phase angle. Here, a frequency range from 1 kHz to 10 MHz is used to define the cost function. Thereby, a thousand points are sampled in the frequency range from 1 kHz to 10 MHz for comparing the modeled and measured impedance. The sampled impedance amplitude and phase angle values are recorded as data sequences formed into four vectors. These four vectors are $\vec{Z}_{\text{cal}}$ for the modeled impedance amplitude, $\vec{Z}_{\text{mes}}$ for the measured impedance amplitude, $\vec{\varphi}_{\text{cal}}$ for the modeled impedance phase angle, $\vec{\varphi}_{\text{mes}}$ for the modeled impedance phase angle.

These vectors are applied to compute the relative amplitude and phase angle errors at each sampling frequency. The outcomes are also recorded as vectors $\vec{\Delta}_{\text{Z}}$ and $\vec{\Delta}_{\varphi}$

$$\vec{\Delta}_{\text{Z}} = \begin{bmatrix} z_1 & z_2 & \cdots & z_n \end{bmatrix}^T \in \mathbb{R}^n \tag{2}$$

$$\vec{\Delta}_{\varphi} = \begin{bmatrix} \varphi_1 & \varphi_2 & \cdots & \varphi_n \end{bmatrix}^T \in \mathbb{R}^n \tag{3}$$

with

$$z_i = \frac{\vec{Z}_{\text{cal}}(i) - \vec{Z}_{\text{mes}}(i)}{\vec{Z}_{\text{mes}}(i)} \in \mathbb{R}$$

$$\varphi_i = \frac{\vec{\varphi}_{\text{cal}}(i) - \vec{\varphi}_{\text{mes}}(i)}{\vec{\varphi}_{\text{mes}}(i)} \in \mathbb{R}.$$

Whereby $\vec{Z}_{\text{cal}}(i)$ is the ith of the vector $\vec{Z}_{\text{cal}}$.

Based on the error vectors $\vec{\Delta}_{\text{Z}}$ and $\vec{\Delta}_{\varphi}$, the classical quadratic cost function [25] is employed with the identity matrix $\mathbf{I}$ with a dimension of n as the cost matrix. By incorporating the weighting factors $w_{|Z|,\text{error}}$ and $w_{\varphi,\text{error}}$, the cost function is expanded as follows:

$$J = w_{|Z|,\text{error}} \cdot \frac{1}{n} \cdot \left\| \vec{\Delta}_{Z} \right\|_{\mathbf{I}}^2 + w_{\varphi,\text{error}} \cdot \frac{1}{n} \cdot \left\| \vec{\Delta}_{\varphi} \right\|_{\mathbf{I}}^2. \tag{4}$$

Besides that, the so-called Pearson distance, which describes the dissimilarity of two data sequences, is also integrated into the cost function, as follows:

$$d(X,Y) = 1 - \frac{\sum_{i=1}^{n}(X_i - \bar{X})(Y_i - \bar{Y})}{\sqrt{\sum_{i=1}^{n}(X_i - \bar{X})^2}\sqrt{\sum_{i=1}^{n}(Y_i - \bar{Y})^2}} \tag{5}$$

whereby:

1) *n:* is the size of data sequence X and Y;
2) X_i, Y_i*:* are the ith element of the sequence X and Y;
3) $\bar{X}, \bar{Y}$*:* are the arithmetic mean of of the data sequences X and Y.

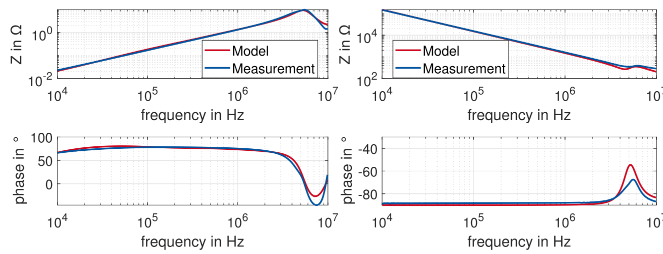

(a) (b)

Fig. 9. Validation of the impedance modeling in the frequency domain and results of some examples. (a) Topology "8-to-9." (b) Topology "0-to-gnd."

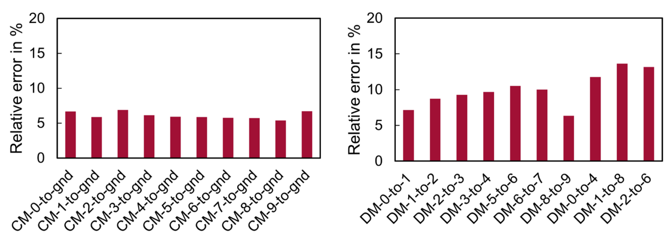

(a) (b)

Fig. 10. Relative errors of the impedance modeling in the frequency domain for different measurement topologies. (a) CM for topologies "turn-to-housing." (b) DM for topologies "turn-to-turn."

Incorporating the Pearson distance is a supplementary metric that avoids the "local minimum trap" and expedites optimization convergence by assessing the similarity degree between the measured and simulated impedance data sequences. In our case, the sample sequence pair $\{X, Y\}$ is determined by sampling the calculated and measured impedance spectrum. Since both the impedance amplitude and phase angle are considered, $\{\overrightarrow{Z}_{\text{cal}}, \overrightarrow{Z}_{\text{mes}}\}$ and $\{\overrightarrow{\varphi}_{\text{cal}}, \overrightarrow{\varphi}_{\text{mes}}\}$ are separately selected for calculating their corresponding Pearson distance. Analogously to (4), two additional weighting factors $w_{|Z|,\text{pearson}}$ and $w_{\varphi,\text{pearson}}$ are introduced. The final design of the cost function is then given by

$$\begin{aligned} J = w_{|Z|,\text{error}} \cdot \frac{1}{n} \cdot \left\| \overrightarrow{\Delta}_{\text{Z}} \right\|_{\mathbf{I}}^2 + w_{\varphi,\text{error}} \cdot \frac{1}{n} \cdot \left\| \overrightarrow{\Delta}_{\varphi} \right\|_{\mathbf{I}}^2 \\ + w_{|Z|,\text{pearson}} \cdot d(\overrightarrow{Z}_{\text{cal}}, \overrightarrow{Z}_{\text{mes}}) \\ + w_{\varphi,\text{pearson}} \cdot d(\overrightarrow{\varphi}_{\text{cal}}, \overrightarrow{\varphi}_{\text{mes}}). \end{aligned} \tag{6}$$

IV. Model Validation in Frequency Domains

The validation of the proposed high-frequency models is initially carried out in the frequency domain. The modeled impedance spectra for different terminal configuration topologies, including "turn-to-turn" and "turn-to-gnd." Fig. 9(a) illustrates the impedance fitting performance of the topology "8-to-9" as an example, and Fig. 9(b) for the topology "0-to-gnd." Fig. 10 presents the statistical results of fitting impedance spectra, including the mean average percentage error (MAPE), defined as

$$\text{MAPE} = \frac{100\%}{N} \sum_{i=1}^{N} \left| \frac{|Z_i| - |\hat{Z}_i|}{|Z_i|} \right| \tag{7}$$

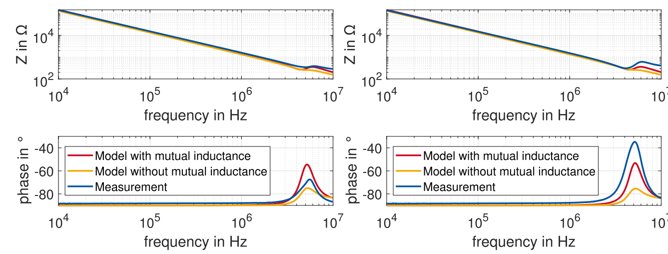

(a) (b)

Fig. 11. Comparing the impedance modeling with and without mutual inductance based on common mode impedance examples. (a) Topology "0-to-gnd." (b) Topology "9-to-gnd."

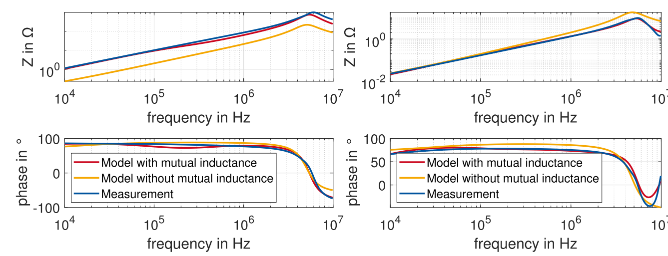

(a) (b)

Fig. 12. Comparing the impedance modeling with and without mutual inductance based on differential mode impedance examples. (a) Topology "0-to-9." (b) Topology "8-to-9."

where the Z_i and $\hat{Z}_i$ represent the measured and modeled impedance at the ith sampled frequency point, and N is the number of sampling points in the frequency domain ranging from $10\,\text{kHz}$ to $10\,\text{MHz}$. In this frequency range, the model achieved a validation average impedance error of 6.09% for the "turn-to-turn" topologies and 11.71% for the "turn-to-gnd" topologies. The average error for all topologies is 9.37%.

A. *Comparison of the Model With and Without Considering Mutual Inductance Between Conductors*

The last part validates the high accuracy of the model with mutual inductances between conductors of the single-tooth winding. This section compares it to the existing model without mutual inductance, as found in the literature. In order to implement the model without any mutual inductances, the mutual inductance value in (1) is defined as zero. All the other setups for impedance fitting are kept the same as in the case of searching parameters for the model with mutual inductance. In the following, some results for identifying the disadvantage of the model without considering mutual inductance are presented.

A comparison between the model with and without considering mutual inductance between conductors is presented in Fig. 11 based on the common mode impedance spectra and in Fig. 12 utilizing the differential mode impedance spectra. The difference between the two kinds of models regarding the common mode impedance is relatively small, up to 2 MHz, and increases obviously above 5 MHz. Overall, the amplitude spectra of the model with mutual inductance fit better to the measured impedance spectra than those without any mutual inductances,

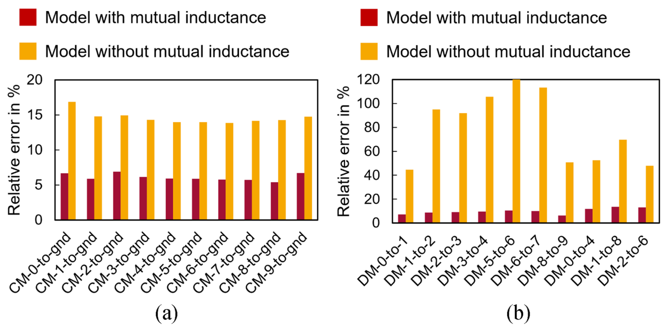

Fig. 13. Relative errors of the impedance modeling in the frequency domain with and without mutual inductance. (a) CM for topologies "turn-to-housing." (b) DM for topologies "turn-to-turn."

TABLE I
PARAMETERS OF THE APPLIED IMPULSE GENERATOR

Parameter	Minimum	Maximum
Voltage amplitude in V	−1200	1200
du/dt in V/ns	1	50
Frequency in Hz	1	100 k

as shown in Fig. 11. In contrast, regarding the differential mode impedance modeling, the deviation of the model without mutual inductance from the measured impedance is evident, as shown in Fig. 12. The modeled impedance for the topology "0-to-9" shows a much lower amplitude than the measured impedance in Fig. 12(a). The reason is the lack of mutual inductance, whose amplitude is in the same order as the self-inductance of the conductors.

A summary of comparing the models with and without mutual inductance is given in Fig. 13(a) for the common mode topologies and in Fig. 13(b) for the differential mode topologies. The model without mutual inductances shows significantly large deviations regarding the impedance spectra, particularly for the differential mode impedance in Fig. 13(b). So far, after the comparative study, the contribution of introducing mutual inductances into the high-frequency model has been verified.

V. VALIDATION OF THE CONDUCTOR-BASED MODEL IN THE TIME DOMAIN

This section validates the proposed gray box model in the time domain. First, the test bench for measuring voltage signals is introduced. Then, the result of validation in the time domain is discussed.

A. Measurement Setup for the Time-Domain Validation

A high-voltage impulse generator consisting of SiC power modules is used for the measurement. For the SiC module, the product "C2M0045170P" of the company Wolfspeed is used. The impulse generator was developed at IEM and initially presented in Hameyer et al.'s [26] work, as shown in Fig. 14.

The voltage impulse generator provides bipolar pulses with duty ratios of 50%. Amplitude, switching frequency, and SR can be varied independently. The range of these parameters can be found in Table I.

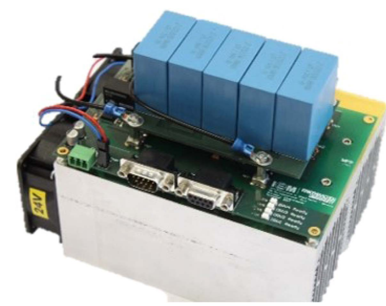

Fig. 14. Developed SiC impulse voltage generator at IEM [26].

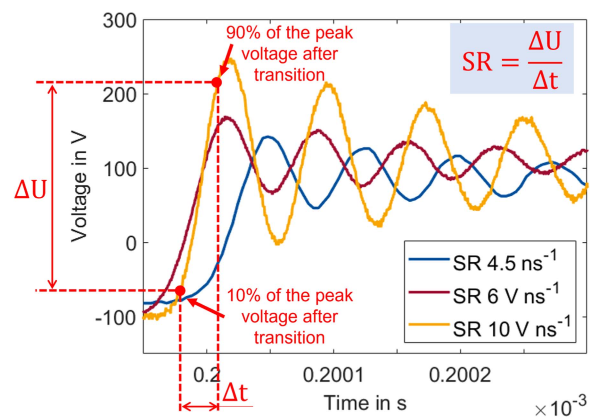

Fig. 15. Voltage signal of the impulse generators with various SRs.

This section uses three impulse generators with different gate resistances for validation. The corresponding voltage SRs include 4.5, 6, and 10 V/ns, as presented in Fig. 15. Thereby, the method of calculating the voltage SR is explained.

This impulse signal serves as the input voltage applied between the two terminals of the winding. For this validation instance, measurement point 0 and the winding housing (GND) are explicitly selected as input. The voltage signals between other measurement points are recorded as output signals, as presented in Fig. 16(b). The measured signals will be compared for validation with the corresponding simulated voltage signals.

B. Model Validation in the Time-Domain

Fig. 17 presents the original and processed measured signal, using the voltage between pacing point 1 and housing as an example. The original measured signals are sampled at a frequency of 2.5 GHz, namely a sampling period of 0.4 ns. In order to reduce signal noise, the measured signals are processed using the Fourier serials method before evaluation. The Fourier serial coefficients of the measured signals are calculated with the switching period as the basis time interval. Then, all the harmonics up to 3000 times the switching frequency are used to reconstruct the measured signals for low-pass filtering. Therefore, the harmonic component of the measured signals shows a maximum frequency of 30 MHz in the case of a 10 kHz switching frequency. In the following, all presented measured signals means after processing with the Fourier methods.

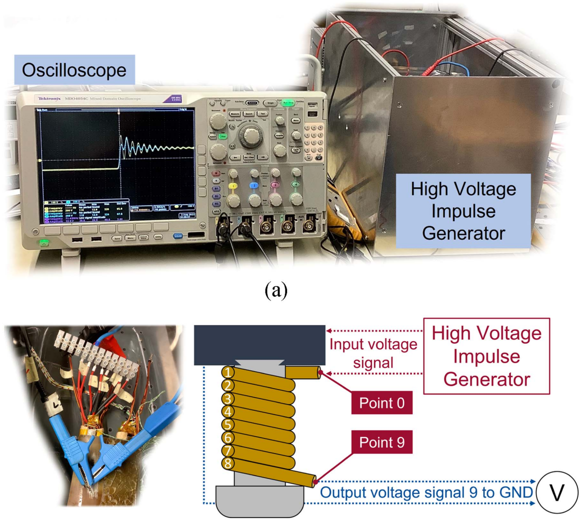

Fig. 16. Measurement setup for the time-domain validation. (a) High voltage impulse generator and oscilloscope. (b) Measurement terminals.

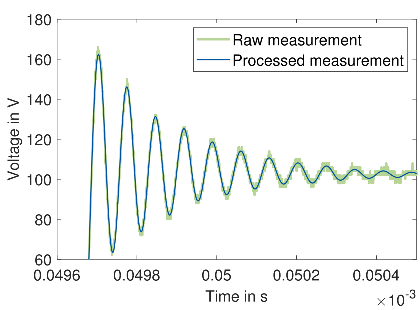

Fig. 17. Raw and processed measured voltage signal for the topology "1-to-gnd" under a SR of 6 V/ns.

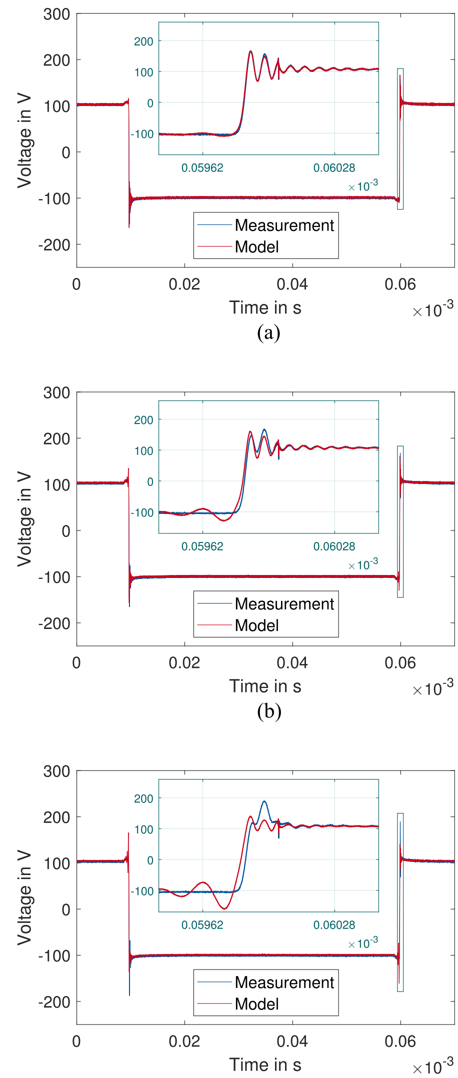

Fig. 18. Model validation using the turn-to-housing voltage signals in the time domain with an SR of 6 V/ns, DC-link voltage of 100 V, and PWM-frequency of 10 kHz. (a) 1-to-gnd. (b) 4-to-gnd. (c) 9-to-gnd.

Fig. 18 presents the measured and modeled turn-to-housing voltage for different outputs. Fig. 18(a) shows an overlapping between the modeled and measured voltage signals to an extreme degree between the pacing point 1 and housing. The overlapping phenomenon in the time domain results from the excellent impedance fitting performance in the frequency domain, as shown in Fig. 10. However, a phase error is identified in Fig. 18(b) since the simulated voltage signal decreases and then increases even though the corresponding measured signal shows an upward transition. The phase error is due to the developed model fitted using impedance spectra up to 10 MHz. However, theoretically, the frequency components of the generated impulse voltage are endless. As a result of the limited impedance fitting range, phase error occurs. This phase error increases along the single-tooth winding from the first turn to the last turn after comparing Fig. 18(c)–(b). One possible explanation is that stator iron is assumed to have equivalent potential based on the preliminary study in Section II-B. In other words, the impedance along the single tooth has not been considered so far. However, The impedance of the tooth iron parts becomes more significant with higher frequency, which may play an essential role in the frequency range above 10 MHz.

As a result of the phase error, the absolute maximum of the simulated voltage signal is relatively smaller than the corresponding measured maximum in Fig. 18(c). In order to solve the problem, the step amplitude in the simulated voltage signal will be used for further evaluation instead of the absolute maximum, as shown in Fig. 19. In this way, the phase error is compensated. Fig. 19 illustrates the calculation of the voltage relative error Δ_{relative} with the compensation considered. Furthermore, the oscillation frequency values during the switching process are also chosen to compare the modeled and measured voltage signals. The oscillation frequency is calculated by analyzing the signal segment following the maximum point of the voltage signal.

Fig. 20 depicts the statistical results of the validation utilizing all turn-to-housing voltage signals by switching frequency 10 kHz and SR 6 V/ns. The peak voltage has an average relative error of 4.47%, and the oscillation frequency has a relative error of 5.09%.

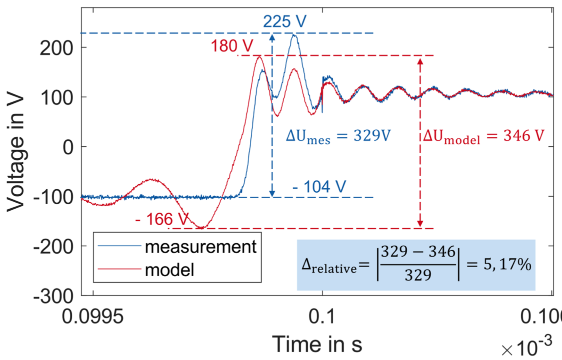

Fig. 19. Comparison between the modeled and measured voltage signals in the time domain for the topology "4-to-gnd," whereby the modeled voltage step value considers the phase error.

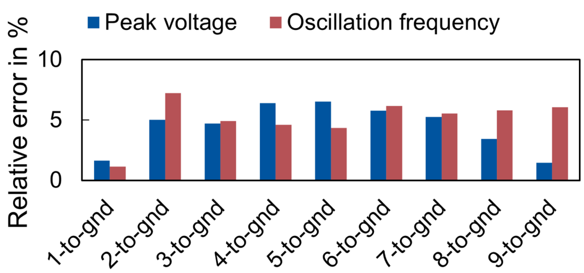

Fig. 20. Relative errors in the time-domain validation using turn-to-housing voltage signals under a SR $6\,\mathrm{V/ns}$, PWM-frequency $10\,\mathrm{kHz}$, and DC-link voltage $100\,\mathrm{V}$.

C. Validation of the Model With Impulse Generators With Higher SRs

Further validation is conducted using another impulse generator with a higher SR of $10\,\mathrm{V/ns}$, potentially posing a more significant challenge to the high-frequency model. The rest of the measurement setup remains the same as before. Fig. 21 illustrates the validation using the typologies "1-to-gnd," "4-to-gnd," and "9-to-gnd" as examples. Compared to the result in Fig. 18 with a lower SR, more pronounced voltage signal fluctuations with higher oscillation frequency are observed. The model captures this heavier oscillation behavior at a higher voltage SR. Fig. 22 displays the statistics of this validation. The peak voltage's relative errors are slightly higher than the case of using the slower slew rate of $6\,\mathrm{V/ns}$. However, the average error in the voltage peak values under the high-voltage SR of $10\,\mathrm{V/ns}$ remains below 6.50%. In addition, the relative average error of the oscillation frequency is 2.70%.

D. Model Validation Under Different PWM Switching Frequencies

Further validations are carried out with various PWM switching frequencies, maintaining an identical SR of $4.5\,\mathrm{V/ns}$ and a dc-link voltage of $80\,\mathrm{V}$. The rest of the configuration remains the same as before.

Fig. 23 presents specific validation results at a PWM frequency of $20\,\mathrm{kHz}$. After comparison, the simulated and measured voltage signals overlap for various topologies to a large degree. Fig. 24 provides an overview of the validation results for all switching frequencies. The overvoltage maximum can be predicted using the gray box model with an average relative error of 2.46% In addition, the oscillation frequency shows an average relative error of 3.95%.

In conclusion, the validation outcomes confirmed the accuracy of the single-tooth winding model under various working

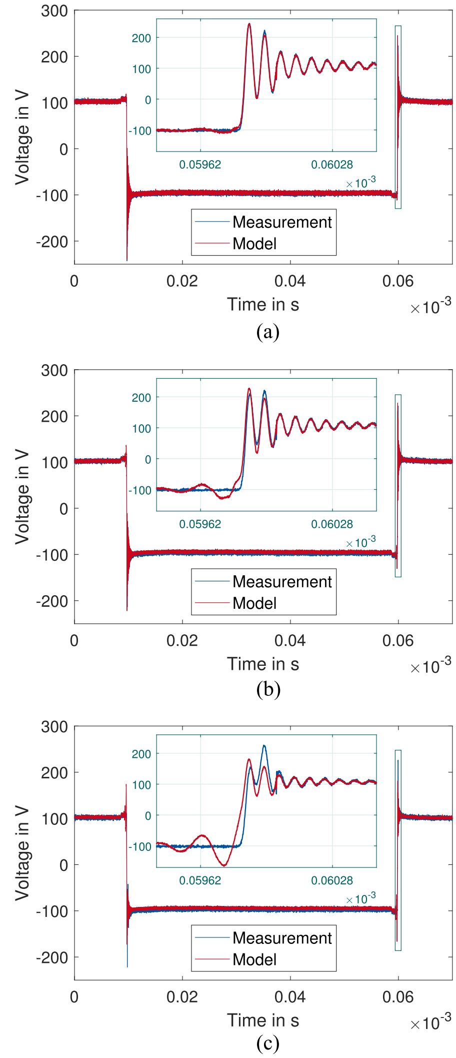

Fig. 21. Model validation using the turn-to-housing voltage signals in the time domain with a voltage SR of $10\,\mathrm{V/ns}$, DC-link voltage of $100\,\mathrm{V}$, and PWM-frequency of $10\,\mathrm{kHz}$. (a) 1-to-gnd. (b) 4-to-gnd. (c) 9-to-gnd.

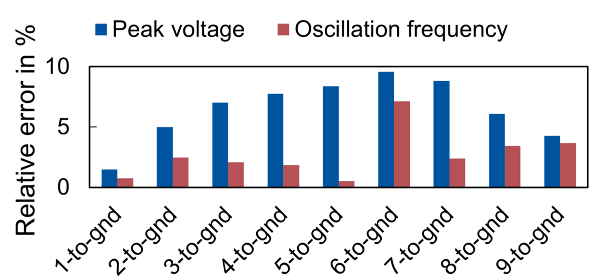

Fig. 22. Relative errors in the time-domain validation using turn-to-housing voltage signals under a voltage SR of $10\,\mathrm{V/ns}$, DC-link voltage of $100\,\mathrm{V}$, and PWM-frequency of $10\,\mathrm{kHz}$.

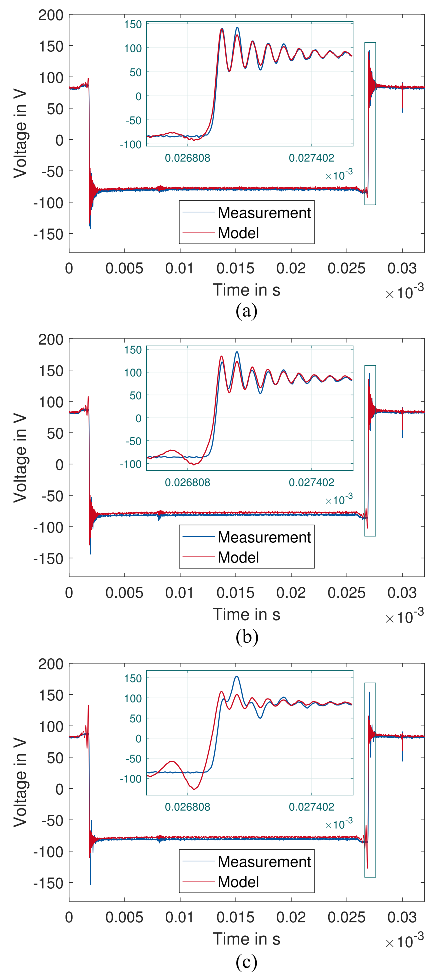

Fig. 23. Validating the model using the turn-to-housing voltage signals with an SR of $4.5\,\mathrm{V/ns}$, DC-link voltage of $80\,\mathrm{V}$, and PWM-frequency of $20\,\mathrm{kHz}$. (a) 2-to-gnd. (b) 4-to-gnd. (c) 9-to-gnd.

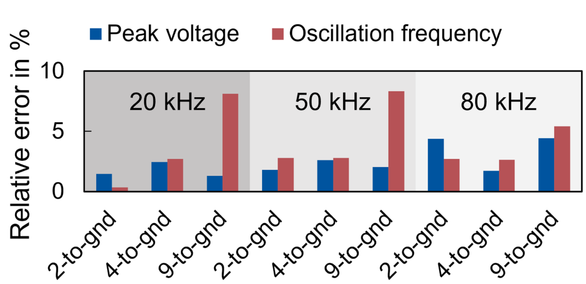

Fig. 24. Relative errors in the time-domain validation using turn-to-housing voltage signals under an SR $4.5\,\mathrm{V/ns}$, DC-link voltage $80\,\mathrm{V}$, and different PWM-frequencies including 20, 50, and 80 kHz.

conditions and demonstrated its potential in predicting overvoltage and voltage distribution. The model can be used to search for suitable gate resistance for the electrical drive and control to reach compromises between lowering switching losses and maintaining the maximum voltage values within a predefined range. Suppose a filter is used to reduce the EMI. In that case, this model can be integrated into the simulation to study the influences of various designs on the maximum voltage values and common mode currents.

VI. Conclusions and Outlooks

A gray box model is used for high-frequency modeling of a single-tooth winding, accounting for frequency-dependent inductive and capacitive coupling. The high-frequency model is validated in the frequency domain, achieving an average relative error of less than 10% across the frequency range from $10\,\mathrm{kHz}$ to $10\,\mathrm{MHz}$. A comparison to the existing model without mutual inductance is made, showing our proposed model's significant improvement. After validation in the frequency domain, the model's accuracy is also verified in the time domain based on test bench measurements. The model is validated under various voltage SRs, switching frequency, and dc-link voltage. The average observed relative error in predicting the maximum voltage is less than 6.50% under all applied different voltage SRs. The oscillation frequency of the voltage during the switching process can be estimated with a mean relative error of less than 5.09% for all cases. Therefore, this model, with its high fidelity and practical implications, can be employed to estimate the maximum voltage stress along the single-tooth winding. This capability holds significant potential for avoiding the overdesign of insulation systems in the next generation of electrical machines. Moreover, it can help adjust modulation and machine control strategies to compromise between lowering power losses and prolonging the electrical machine's lifetime.

References

[1] A. M. EL-Refaie, "Fractional-slot concentrated-windings synchronous permanent magnet machines: Opportunities and challenges," *IEEE Trans. Ind. Electron.*, vol. 57, no. 1, pp. 107–121, Jan. 2010.

[2] I. Petrov, M. Polikarpova, P. Ponomarev, P. Lindh, and J. Pyrhönen, "Investigation of additional ac losses in tooth-coil winding PMSM with high electrical frequency," in *Proc. XXII Int. Conf. Elect. Machines*, 2016, pp. 1841–1846.

[3] H. Kono et al., "Improving the specific on-resistance and short-circuit ruggedness tradeoff of 1.2-kV-class SBD-embedded SiC MOSFETs through cell pitch reduction and internal resistance optimization," in *Proc. 33 rd Int. Symp. Power Semicond. Devices ICs*, 2021, pp. 227–230.

[4] P. Brauer, "High-frequency voltage distribution modelling of a slotless pmsm from a machine design perspective," Ph.D. dissertation, KTH Roy. Inst. Technol., Stockholm, Sweden, 2018. [Online]. Available: http://urn.kb.se/resolve?urn=urn:nbn:se:kth:diva-224174

[5] P. Vijayraghavan and R. Krishnan, "Noise in electric machines: A review," *IEEE Trans. Ind. Appl.*, vol. 35, no. 5, pp. 1007–1013, Sep./Oct. 1999.

[6] F. Chiang, "Effects of high frequency voltage stress on air insulation and solid insulation," in *Proc. IEEE Symp. Product Compliance Eng. Proc.*, 2010, pp. 1–10.

[7] H. Zeng, J. Swanke, T. M. Jahns, and B. Sarlioglu, "High-frequency modeling and inter-turn voltage distribution analysis of a modular electric machine for electric aircraft propulsion," in *Proc. IEEE Transp. Electrific. Conf. Expo*, 2022, pp. 1097–1104.

[8] Y. Xu et al., "Impact of high switching speed and high switching frequency of wide-bandgap motor drives on electric machines," *IEEE Access*, vol. 9, pp. 82866–82880, 2021.

[9] R. Kerkman, D. Leggate, and G. Skibinski, "Interaction of drive modulation and cable parameters on ac motor transients," in *Proc. Conf. Rec. IEEE Ind. Appl. Conf. 31st IAS Annu. Meeting*, 1996, vol. 1, pp. 143–152.

[10] M. Ghassemi, "Accelerated insulation aging due to fast, repetitive voltages: A review identifying challenges and future research needs," *IEEE Trans. Dielectr. Electr. Insul.*, vol. 26, no. 5, pp. 1558–1568, Oct. 2019.

[11] O. Magdun, S. Blatt, and A. Binder, "Calculation of stator winding parameters to predict the voltage distributions in inverter fed AC machines," in *Proc. 9th IEEE Int. Symp. Diagnostics Electric Machines, Power Electron. Drives*, 2013, pp. 447–453.

[12] A. Boglietti and E. Carpaneto, "Induction motor high frequency model," in *Proc. Conf. Rec. IEEE Ind. Appl. Conf. 34th IAS Annu. Meeting*, 1999, vol. 3, pp. 1551–1558.

[13] S. Yang, L. Zhai, and G. Hu, "Measurement-based modeling of high frequency equivalent circuit of permanent magnet synchronous motor of electric vehicle," in *Proc. Asia-Pacific Int. Symp. Electromagn. Compat.*, 2022, pp. 719–721.
[14] A. Rahimi and K. Kanzi, "Improved high-frequency modeling of PMSM using 3-D finite element analysis," in *Proc. Int. Power Syst. Conf.*, 2019, pp. 71–78.
[15] D. Zheng, G. Lu, and P. Zhang, "An improved online stator insulation monitoring method based on common-mode impedance spectrum considering the effect of aging position," *IEEE Trans. Ind. Appl.*, vol. 58, no. 3, pp. 3558–3566, May/Jun. 2022.
[16] S. Sundeep, J. Wang, and A. Griffo, "Holistic modeling of high-frequency behavior of inverter-fed machine winding, considering mutual couplings in time domain," *IEEE Trans. Ind. Appl.*, vol. 57, no. 6, pp. 6044–6057, Nov./Dec. 2021.
[17] R. Stoll, *The Analysis of Eddy Currents, Ser. Monographs in Electrical and Electric Engineering*. Oxford, U.K.: Clarendon Press, 1974.
[18] K. Abdennadher, P. Venet, G. Rojat, J.-M. Rétif, and C. Rosset, "A real-time predictive-maintenance system of aluminum electrolytic capacitors used in uninterrupted power supplies," *IEEE Trans. Ind. Appl.*, vol. 46, no. 4, pp. 1644–1652, Jul./Aug. 2010.
[19] B. H. Lin, J. T. Tsai, and K. L. Lian, "A non-invasive method for estimating circuit and control parameters of voltage source converters," *IEEE Trans. Circuits Syst. I: Regular Papers*, vol. 66, no. 12, pp. 4911–4921, Dec. 2019.
[20] V. Karakaşll, F. Gross, T. Braun, H. D. Gersem, and G. Griepentrog, "High-frequency modeling of delta- and star-connected induction motors," *IEEE Trans. Electromagn. Compat.*, vol. 64, no. 5, pp. 1533–1544, Oct. 2022.
[21] B. Heidler, K. Brune, and M. Doppelbauer, "High-frequency model and parameter identification of electrical machines using numerical simulations," in *Proc. IEEE Int. Electric Machines Drives Conf.*, 2015, pp. 1221–1227.
[22] A. Hoffmann and B. Ponick, "Method to predict the non-uniform potential distribution in random electrical machine windings under pulse voltage stress," *Energies*, vol. 15, no. 1, 2022, Art. no. 358.
[23] H. Peng et al., "High-frequency modeling of permanent magnet synchronous machines using grey box models," *IEEE Trans. Transport. Electrific.*, to be published: doi: 10.1109/TEC.2024.3370800.
[24] H. Peng et al., "Voltage distribution modeling along stator windings in permanent magnet synchronous machines using coil-based grey box models," *IEEE Trans. Energy Convers.*, to be published, doi: 10.1109/TEC.2024.3370800.
[25] S. Boyd and L. Vandenberghe, *Convex Optimization*. Cambridge, U.K.: Cambridge Univ. Press, 2004.
[26] K. Hameyer, A. Ruf, and F. Pauli, "Influence of fast switching semiconductors on the winding insulation system of electrical machines," in *Proc. Int. Power Electron. Conf.*, 2018, pp. 740–745.

Hujun Peng received the bachelor's degree from Zhejiang University, Hangzhou, China, in 2013, and the master's degree from the Dresden University of Technology, Dresden, Germany, in 2017, both in electrical engineering. He received the Ph.D. degree in electrical engineering from RWTH Aachen University, Aachen, Germany, in 2023.

Since 2018, he has been a Research Assistant with the Institute of Electrical Machines, RWTH Aachen University. Since 2023, he has been a Postdoctoral Researcher with the Institute of Electrical Machines, RWTH Aachen University. His research interests include high-frequency modeling of electrical machines, energy management of fuel cell hybrid vehicles, characterization of insulation systems in electric machines, and the analysis of parasitic effects in electric drives.

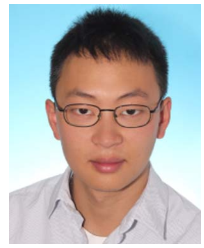

Yue Yu received the master's degree in automation engineering with a specialization in mechatronics from RWTH Aachen University, Aachen, Germany, in 2023.

He commenced his tenure as a Student Assistant with the Institute of Electrical Machines, RWTH Aachen University, in 2023. His research interests include high-frequency modeling of electrical machines.

Kay Hameyer (Senior Member, IEEE) received the M.Sc. degree in electrical engineering from the University of Hannover, Hanover, Germany, in 1986, and the Ph.D. degree in electrical engineering from the University of Technology Berlin, Berlin, Germany, in 1992, for working on permanent magnet excited machines.

He was a Design Engineer for permanent magnet servomotors with Robert Bosch GmbH, Stuttgart, Germany. From 1988 to 1993, he was a Member of staff with the University of Technology Berlin. From 1996 to 2004, he was a Full Professor of numerical field computations and electrical machines with Katholieke Universiteit Leuven, Leuven, Belgium. Since 2004, he has been a Full Professor and the Director of the Institute of Electrical Machines (IEM), RWTH Aachen University, Aachen, Germany. The characterization and modeling of hard- and soft-magnetic materials is another focus of his work. He has authored or coauthored more than 350 journal publications, more than 700 international conference publications, and four books. His research interest focuses on all aspects of the design, control, and manufacturing of electrical machines and the associated numerical simulation. His research interests include numerical field computation and optimization, the design and control of electrical machines, in particular, permanentmagnet excited machines, and induction machines.

Dr. Hameyer is a Member of the German VDE and a Fellow of the Institution of Engineering and Technology, U.K.